ORIGINAL PAPER

Observing Geomorphological Change on an Evolving Coastal Sand Dune Using SLAM-Based UAV LiDAR

Jeremy Sofonia[1] (ORCID) · Stuart Phinn[1] · Chris Roelfsema[1] · Farid Kendoul[2]

Abstract

Following over 20 years of manned airborne LiDAR in the remote sensing of geomorphological change in coastal environments, rapid advancements in unmanned aerial vehicle (UAV) technologies have expanded the possibilities of acquiring very high-resolution data efficiently over spatial-temporal scales not previously feasible. This study employed a new Simultaneous Localisation and Mapping (SLAM)–based LiDAR system ("Hovermap") across a segment of coastal sand dune of Bribie Island, Queensland, Australia. The study area was identified by the local council as an area of interest over concern that continued erosion at an existing blowout could result in cutting off northern Bribie Island and adversely affect hydrodynamic processes of Pumicestone Passage, its shoreline, and its associated infrastructure. Here, we employed the Hovermap within a multi-temporal design in which four, quarterly, surveys undertaken over a 9-month period from July 2017 to April 2018. On the first survey, a Leica P40 (P40) terrestrial laser scanner (TLS) was also deployed across the study area to facilitate a performance comparison. Hovermap reported a mean point cloud density of 2532 ± 170 pts.·m^{-2}, ground sample distance (GSD) of 0.02 ± 0.001 m, and RMSE of 0.050 ± 0.31 m relative to ground control points (GCPs). Three-dimensional mesh objects were derived from all point clouds obtained and evaluated in terms of elevation and slope with mesh-to-mesh deviations and volumetric change (cubature) analysis examined over consecutive surveys. The Hovermap closely matched results of the P40 with measures of elevation and slope differing by approximately 2% and 7%, respectively. Mean vertical deviation (0.01 ± 0.03 m) and cubature (~ 2.5 m^3 net difference) results also showed close agreement. Due to stable wave conditions between the first three surveys, minimal changes in beach topography were observed, whilst pronounced erosion and scarping of the foredune were measured during the final survey. This erosion was evidenced from changes in mean elevation ($- 16\%$), slope ($+ 25\%$), and deviation ($+ 86\%$) relative to the mean measurements over the first three survey dates. In addition, a net loss of approximately -1295 m^3 of sand was measured between the final two survey dates (January–April 2018). This is supported by local marine weather data in which a significant increase in local wind speeds (ANOVA, $F(1,180) = 6.257$, $p = 0.013$) and wave heights (ANOVA $F(1,180) = 41.769$, $p \leq 0.001$) were recorded over the same interval. The results presented here are first to demonstrate that UAV LiDAR performance was robust in a typical, moderate-energy, sandy beach and is suited for the detection and evaluation of coastal morphologic change at microspatial and temporal scales.

Keywords LiDAR · Drone · Coastal sand dunes · Geomorphology

1 Introduction

Dune management is considered a prime coastal management tool [60] and whilst prior monitoring efforts to capture fine-scale features required laborious field surveys over relatively limited spatial scales (due to the intensive labour requirements) [35, 59], the past two decades have shown marked advances in describing, and quantifying, the dynamic processes

✉ Jeremy Sofonia
   j.sofonia@uq.edu.au

   Stuart Phinn
   s.phinn@uq.edu.au

   Chris Roelfsema
   c.roelfsema@uq.edu.au

   Farid Kendoul
   farid@emesent.io

1 Remote Sensing Research Centre, School of Earth and Environmental Sciences, University of Queensland, St Lucia, QLD 4072, Australia
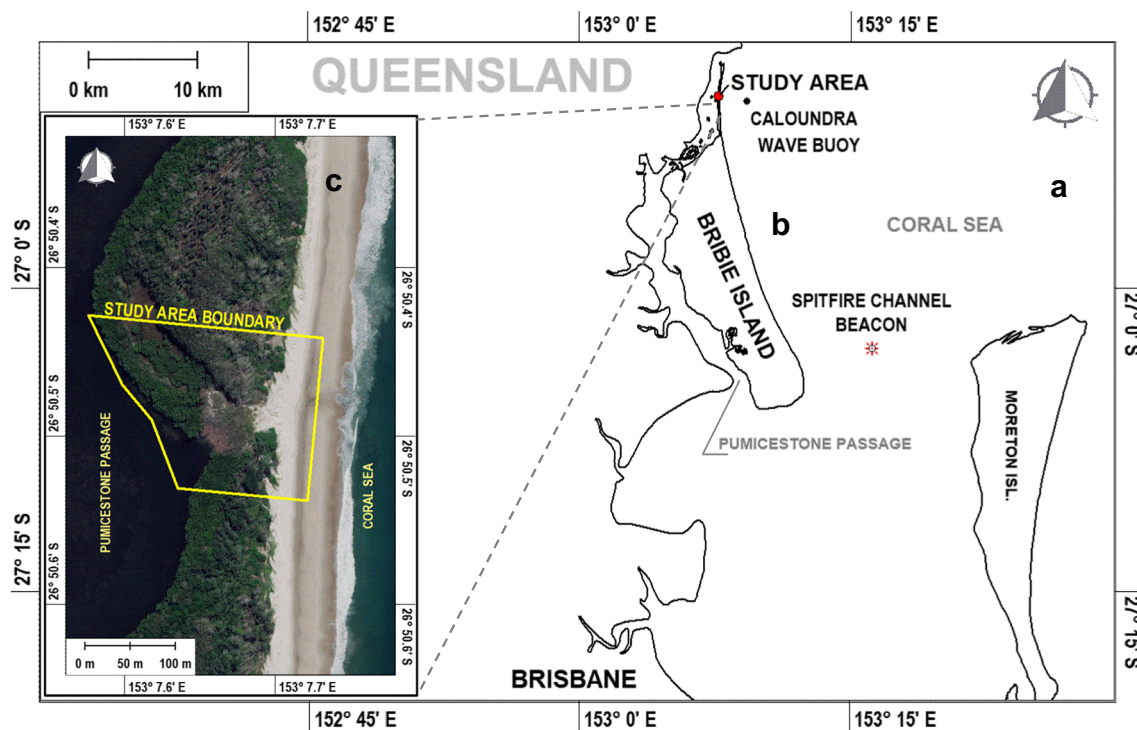
2 Emesent Pty Ltd, Pullenvale, QLD 4069, Australia

Fig. 1 Location of the study area (A) on the Pacific coast of Queensland, Australia, along the (B) northern Bribie Island beach. (C) Inset of the *Study Area* (MGA Projection, GDA 94 Datum). Photo source: Esri World Imagery July 2017

affecting coastal beach and estuarine systems. From the early works of Brock et al. [9], Gutierrez et al. [29], and Stockdon et al. [59], airborne light detection and ranging (LiDAR) (from manned aircraft) has been increasingly used and become an important tool in coastal geomorphology through facilitating the acquisition of detailed, and accurate, topographic data over broad coastal regions and enabling geomorphic analysis over a continuum of scales [29]. Mitasova et al. [45], for example, utilized airborne multi-temporal LiDAR to detect, analyse, and quantify topographic changes in rapidly evolving coastal landscapes. Similarly, the robust studies of Revell et al. [50], Allen et al. [7], and Loftis et al. [43] utilized airborne LiDAR for coastal terrain modelling and change detection. More recently, Dong [20] employed airborne LiDAR and terrain modelling to automate measures of dune migration whilst Brownett and Mills [12] and Lalimi et al. [39] have combined airborne LiDAR with hyperspectral imagery to map and classify vegetation patterns in coastal dunes.

As the costs associated with airborne LiDAR have declined, the use has increased as evidenced by Brock and

Purkis [10] and such studies as Claudino-Sales et al. [16], Splinter et al. [58], and Turner et al. [62] who utilized airborne LiDAR data, flown pre- and post-storm events, to understand, and predict, along-shore variable sand dune erosion. As expressed by Pikelj et al. [49], however, airborne LiDAR from manned aircraft can remain prohibitively expensive and thereby potentially limit temporal-coverage. As technology has advanced, however, the utilization of unmanned aerial vehicles (UAVs) in coastal monitoring has increased and are proving to be an efficient, cost-effective, tool for topological mapping and measurement with deployment flexibility and spatial-temporal resolution ('microscales' [54]) not previously feasible within the coastal zone [21, 62]. To date, studies utilizing UAVs have focused almost exclusively on the use of structure from motion photogrammetry (SfM) and whilst this has shown to be very effective in creating, detecting, and measuring change using Digital Surface Models (DSMs) with sub-metre resolution [26, 33, 48, 53, 61], such studies may be somewhat limited by the

Fig. 2 Northerly ground perspective of the study area centred on the blowout and overwash fan formation that bisects this relatively narrow (~ 150 m) part of northern Bribie Island

Table 1 Timing of surveys and intervals between each event within this study

Event	New moon	Survey date	Survey *Interval* (duration)
Survey1	23 July 2017	28 July 2017	–
Survey2	20 October 2017	25 October 2017	*Interval1* (88 days)
Survey3	17 January 2018	23 January 2018	*Interval2* (89 days)
Survey4	16 April 2018	24 April 2018	*Interval3* (91 days)

characteristics of the surface being measured, presence of vegetation, water, and small-scale texture contributing to inaccuracies [17, 34].

Unlike that of the SfM approach, UAV LiDAR is not restricted to the development of DSMs but is able to 'penetrate' dune vegetation for the development of accurate Digital Terrain Models (DTMs) and facilitate a more direct measure of dune structure relative to local processes driving geomorphic change. In addition, the high spatial resolution and capacity for regular monitoring, UAV LiDAR could better inform morphodynamic and beach dune erosion models, important to coastal scientists and engineers and provide the theory, data, models, and predictions that planners, managers, and policymakers require [54].

Whilst traditional point cloud methods are suitable for monitoring change in beach topography [21], here we describe, test, and evaluate a new approach in the deployment of UAV LiDAR across an existing blowout feature along the coastal dunes of northern Bribie Island, Queensland. Southeast Queensland is considered one of the coastal 'hotspots' in Australia due to increasing population pressures and threat of rising sea levels due to ocean thermal expansion [15] and the Sunshine Coast City Council (SCCC) has identified our study location as an area of concern where further degradation of the existing blowout could result in ocean flow-through to Pumicestone Passage, adversely affecting local hydrodynamic characteristics of navigable waters.

Here, we describe a methodology that, if expanded upon with further research, could provide a new tool for coastal survey applications on micro- to mesoscales (as defined by Sherman and Bauer [54]) and facilitate opportunities to ask new questions regarding the processes affecting observed changes. In addition, results from this study provide a quantitative performance assessment of the Hovermap LiDAR within a dynamic environment and assist in identifying the strengths, and limitations, of this system in the acquisition of accurate 3D point clouds associated with coastal survey and mapping research and monitoring.

2 Materials and Methods

2.1 Study Area Location and Timing

Bribie Island is the northernmost, and smallest, of the major sand islands of the Moreton Bay Marine Park, Queensland, Australia (Fig. 1(A)) and is part of an internationally recognized Ramsar wetland and migratory shorebird habitats [1]. Located approximately 70 km north of Brisbane in eastern Australia, Bribie Island (Fig. 1(B)) is separated from the mainland by Pumicestone Passage, characterized by intertidal mangrove and saltmarsh habitat, whilst the 34-km western shoreline along the Coral Sea (Southwest Pacific Ocean) consists of sandy beach and coastal dune formations [15]. Most of the island is designated as a National Park and Recreation Area (~ 5580 ha) with four-wheel drive (4WD) and camping activities allowed with corresponding access permits [2].

The *Study Area* (26° 50.5′ S, 153° 7.7′ E) corresponds to a segment of coastal sand dune along northern Bribie Island where washover processes have compromised the dune structure and foredune vegetation as evidence by an existing blowout and overwash fan formations (Fig. 1(C) and Fig. 2). This relatively narrow (~ 150 m wide) portion of the island was identified by the SCCC as an area of concern in that continued

Fig. 3 Example imagery of the **a** laser registration targets and **b** Leica GS16 GNSS antenna with CS20 controller utilized to georeferenced and co-reference individual laser scans

(a)

(b)
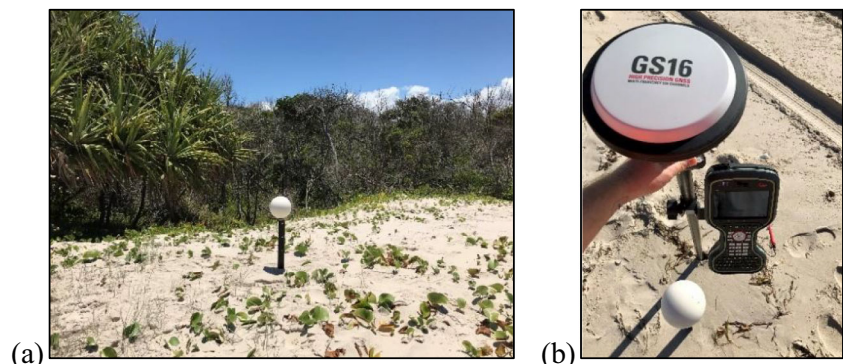
erosional processes might cut off northern Bribie Island and alter hydrodynamic processes of the adjacent waters of Pumicestone Passage, its shoreline, and associated infrastructure (e.g. adversely affect established navigation channels). With increased monitoring focus, this location represents ideal testbed for evaluating the utility of new monitoring techniques at microscales such as UAV LiDAR.

To observe temporal variation across microscales [54], four surveys were conducted every 3 months (quarterly) from July 2017 to April 2018 (Table 1). The timing of this study was designed to commence prior-to, and run through, the official 'cyclone season' (1 November to 30 April). In effort to minimize variability in coastline exposure due to tidal regime, each survey was undertaken 5 days following the new moon with the exception of *Survey4*, which was delayed 3 days due to a local storm event. All UAV flights were executed in the mid-to-late afternoon to coincide with the falling tide in effort to minimize variability in beach exposure during the tidal cycle.

2.2 Georeferencing and Co-registration

Given that the coastal dunes on Bribie Island are a dynamic environment, it was not practical to establish fixed ground control points (GCPs) over the duration of this study. As such, each scanning event was preceded by the placement of six (7.5 cm) laser registration targets across the study area. Targets were representatively distributed with three across the foredune and dune crest, respectively. A Leica Viva GS16 GNSS 'Smart Antenna' with CS20 Controller (Leica [4])[1] was used in combination with a connection to the Geoconnect SmartnetAUS RTK (Real-Time Kinematic) network to georeference each target in the MGA projection, GDA 94 Datum with a < 20-mm 3D solution (Fig. 3). The GCPs were later utilized to co-register individual scans and facilitate comparative analysis.

2.3 Leica P40

Similar to the work of Fabbri et al. [23] and Zhou et al. [71], a Leica P40 terrestrial laser scanner (P40) [41][2] was utilized to capture a high-definition, high accuracy 3D image of the *Study Area,* and serve as a comparative 'baseline', just prior to the UAV flight during *Survey1*, like that of Elsner et al. [21]. With a reported range accuracy of ± 1.2 mm, 3D position accuracy of 3 mm (at 50 m) and scan rate up to 1,000,000 pts.·s^{-1}, the P40 was deployed at nine locations, three along beach seaward of the foredune, three on the dune crest, and

three within the central hind-dune complex. Individual scans were then co-referenced, unified, and cropped to retain only points within the S*tudy Area* boundary using the Leica Cyclone 3D Point Cloud Processing Software (v.8.1.1).

2.4 Hovermap and UAV Platform

Initially described by Kaul et al. [36], the Hovermap is a lightweight (1.5 kg) 3D LiDAR mapping payload specifically designed for small UAV platforms. Utilizing a proprietary Simultaneous Localisation and Mapping (SLAM) solution to generate 3D point clouds Hovermap does not require GNSS and therefore not subject to the same challenges as other systems that are dependent on satellite-derived positional information [66]. Although not dependent on GNSS and IMU sensor data to generate point clouds, the Hovermap was connected to, and utilized information from, the onboard GNSS system of the UAV platform (± 0.5 m vertical, ± 1.5 m horizontal) to facilitate georegistration.

Here, the Hovermap [22][3] was deployed using the Velodyne (VLP-16) 'Puck-LITE' sensor. The VLP-16 is a 16-channel dual-return sensor with a scan rate up to 600,000 pts.·s^{-1}, angular resolution (vertical) of 2.0°, field-of-view (FOV) along the z-axis of 360° × 30°, reported accuracy of $\pm .03$ m, and range up to 100 m [64].[4] As integrated on the Hovermap, the VLP-16 is also rotated 360° about the y-axis at a rate of 0.5 Hz effecting a near 360° × 360° field-of-view of the surrounding environment, irrespective of the direction of travel, other than where obstructed (e.g. by the UAV).

All flights were conducted using a DJI 'Matrice (M600) Pro' UAV platform (DJI Science & Technology, China),[5] capable of flight times with the Hovermap between 20 and 25 min. As a self-contained unit, the Hovermap is easily integrated onto any suitable UAV platform and was secured to the M600 in this study using a straightforward anti-vibration mount to minimize the potential influence of high-frequency vibration (Fig. 4).

2.5 Flight Planning

Previous work by Sofonia et al. [57] concluded that the range of the Hovermap was (i.e. altitude of the UAV) the single most important variable with regard to point cloud density and accuracy, with the best overall performance observed at relatively low altitudes. Based on this, and on the previous work of Wallace et al. [65], flight altitudes for all surveys was set to 20 m above the beach ground level. This effectively minimized the UAV altitude whilst maintaining a safe separation from trees established in the hind-dune complex. To maximize

---

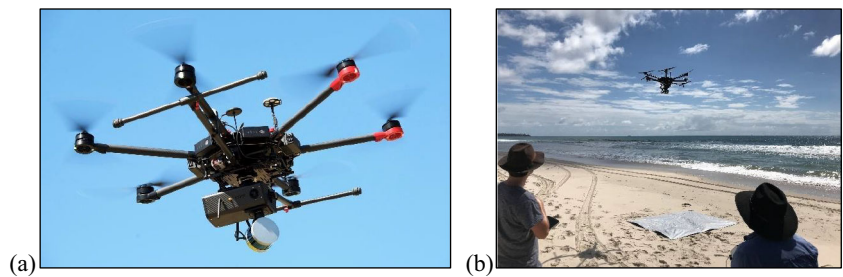[1] Leica Viva GS16: https://leica-geosystems.com/products/gnss-systems/smart-antennas/leica-viva-gs16
[2] Leica P40: https://leica-geosystems.com/products/laser-scanners/scanners/leica-scanstation-p40%2D%2Dp30

[3] Hovermap: https://emesent.io/products/
[4] Velodyne VLP-16: https://velodynelidar.com/vlp-16.html
[5] DJI M600 Pro: https://www.dji.com/au/matrice600-pro

point cloud density and the number of ground returns through vegetation, a 'cross-flight' similar to that as discussed by Gerke and Przybilla [24] was employed. Flight speed was set for each flight at 4 m·s^{-1} as determined as the minimum speed required to cover the estimated distance travelled in a cross-flight pattern over the *Study Area* (~ 4750 m^2) within a conservative estimate of the maximum UAV flight time (20 min).

Each flight was planned using a geo-referenced Esri World Imagery aerial photograph of the study area and Global Mapper (v.18.2, Blue Marble Geographics, USA) software. To maximize point cloud density and canopy 'penetration', flight lines were plotted at 20 m intervals using the Grid tool to create the 'cross-flight' pattern (Fig. 5a). Exported as *.kml files, these waypoints were imported into the Autopilot software (v.3.8, Hangar Technology, USA) used to control the UAV with speed and altitude set as previously described (Fig. 5b).

2.6 Marine Weather

To better understand the process forcing observed geomorphological change within the *Study Area*, marine wind and wave data were obtained from the nearest relevant monitoring stations covering the duration of the study [68]. Specifically, wind speed and direction measurement recorded every 3 h

were sourced from the Australian Government Bureau of Meteorology 'Spitfire Channel' Weather Beacon (040927) [3] located (27° 2.9′ S, 153° 16.0′ E) approximately 27 km southeast (brg. 148° 35.8′) of the *Study Area*. Similarly, half-hourly significant wave height measures were obtained from the Queensland Government Coastal Impacts Unit, 'Caloundra' Wave Monitoring Buoy [5] located (26° 50.8′ S, 153° 9.3′ E) approximately 2.6 km east (brg. 100° 28.5′) of the *Study Area* (Fig. 1). Daily averages were calculated for all values to facilitate analysis with groups of the same size (n) for each interval, a term used here as the time between survey events.

2.7 Initial Data Processing

Sofonia et al. [57] describe method for pre-processing UAV LiDAR point clouds with the Python3 coding language [63] and discuss several benefits in doing so including a standardized approach to the removal of noise and other undesired points and improved basis for inter-flight comparisons. This script was employed here with the parameters listed in Table 2. Point clouds were subsequently filtered and cropped as illustrated in Fig. 6. Descriptive statistics for each flight were recorded including altitude (m), speed (m·s^{-1}), and area (m^2) as well as resulting point cloud density (pts.·m^{-2}), ground
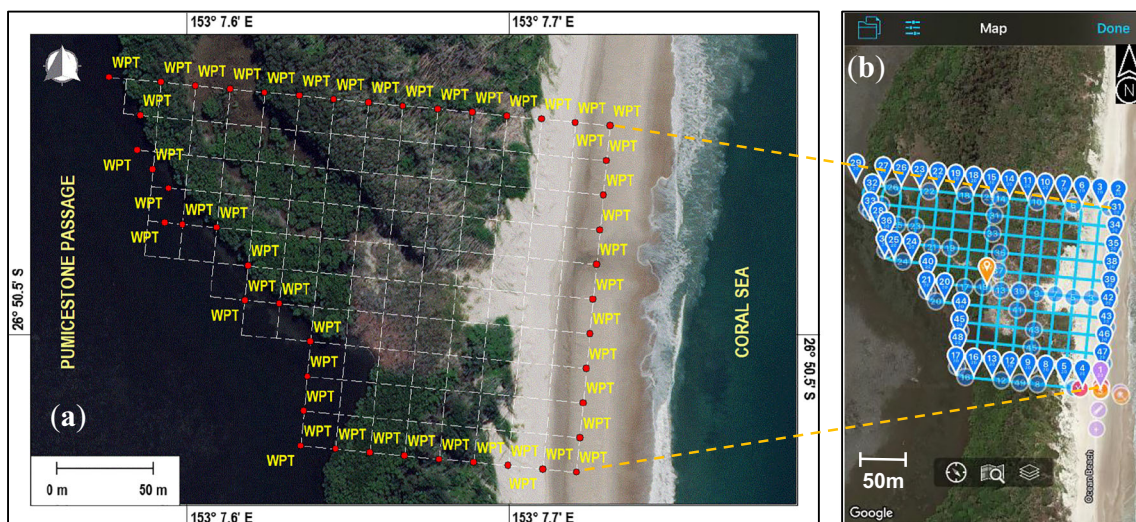

Fig. 5 Screen captures of autonomous 'cross-flight' planning for (**a**) in Global Mapper (MGA Projection, GDA 94 Datum, photo source: Esri World Imagery July 2017) with the (**b**) corresponding flight plan as loaded in the Hangar Autopilot software

Table 2 Key parameter settings utilized in data pre-processing across all flights using the Python script described by Sofonia et al. [57]

Parameter	Description	Setting
ε	Tolerance: aggressiveness of ascent/decent cropping	0.0
$Vert_n$	Number of vertices to create bounding polygon	250
FOV_{angle}	Point restriction by field-of-view angle (°)	Disabled
r_{min}/r_{max}	Minimum/maximum range to keep points (m)	0.0/50
n_{SOR}	Number of standard deviations above local mean to remove points	2.0
k_{SOR}	Number of points used to compute the mean distance to nearest neighbour	8.0
$Alt._{radius}$	Radius of which to include points to use when calculating altitude (m)	1.0

sample distance (GSD, m), and 'sampling effort variable' (SEV, s·m^{-2}).

The unified cleaned and cropped P40 and Hovermap data were imported into CloudCompare (v.2.10 alpha) [25] wherein the initial georeferencing of the point clouds was achieved by utilizing the GPCs from each survey and the Align (point pairs picking) tool. As the accuracy of this process is dependent on how well each point is selected relative to the corresponding GCP, this process was repeated until the final root mean square error (RMSE) was as low as possible ($\bar{x}$ = 0.050 ± 0.031 m). Each georeferenced point cloud was then brought into Global Mapper and cropped to the *Study Area* boundary (Fig. 7a). Given the objective of this study was to evaluate the ability of the Hovermap to detect microscale change in local geomorphology, the point cloud was spatially constrained to focus on that part of the *Study Area* that was likely to experience significant elevation changes [11] over relatively short time scales (i.e. months). Illustrated in Fig. 7b, this area is termed here as the *Analysis Area* and represents the portion of data exported to 3DReshaper (3DR) 3D scanning software package (v.17.0.24477.0, Technodigit, France) for further interrogation.

2.8 Terrain Modelling

Primarily interested in temporal changes of the foredune stoss slope and beach surface, the Ground Extractor tool within 3DR was utilized to classify and retain only 'ground-points' and, similar to previous studies [7, 27, 43, 45], create DTMs of the *Analysis Area*. Here, DTMs were created using a slope setting of 55°, 'local steep slopes' strategy and refined using an average point distance of 0.020 m as derived from the observed mean GSD of the Hovermap point clouds (Fig. 8).

2.9 Elevation, Slope, Deviation, and Cubature

Elevation and slope have long been common data sets for assessing the basic structure of sand dunes [42, 51, 54, 55, 67] with change detection a key monitoring aspect of understanding, modelling, and modelling geomorphic change [23, 45, 47, 59, 69]. The use of mesh DTMs (or similar) for this type of inspection has been in use since at least 2003 [46] and is now a relatively standard approach with continued improvement in software capability and PC performance [6, 23, 34, 40, 43, 71].

Fig. 6 Example outputs (local coordinate projection) from *Survey1* (coloured by *range*) illustrating (**a**) the original point cloud and (**b**) points retained post-processing with the Python script described
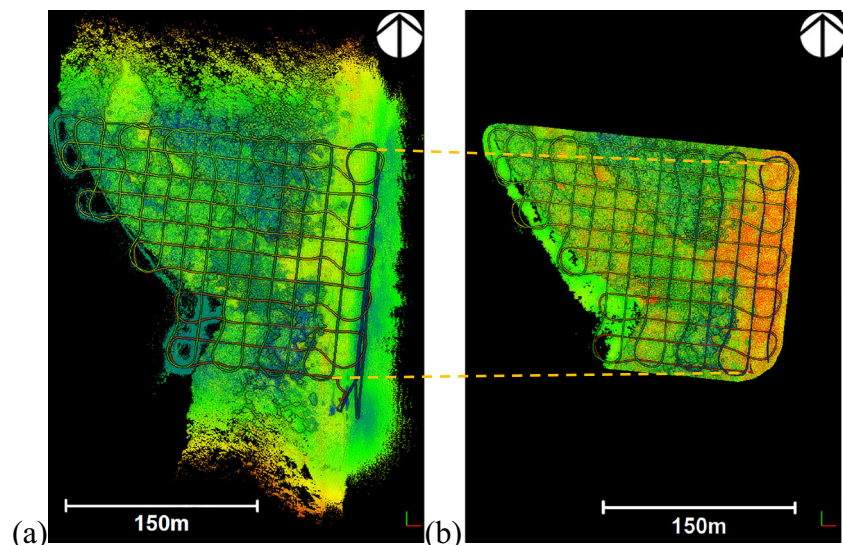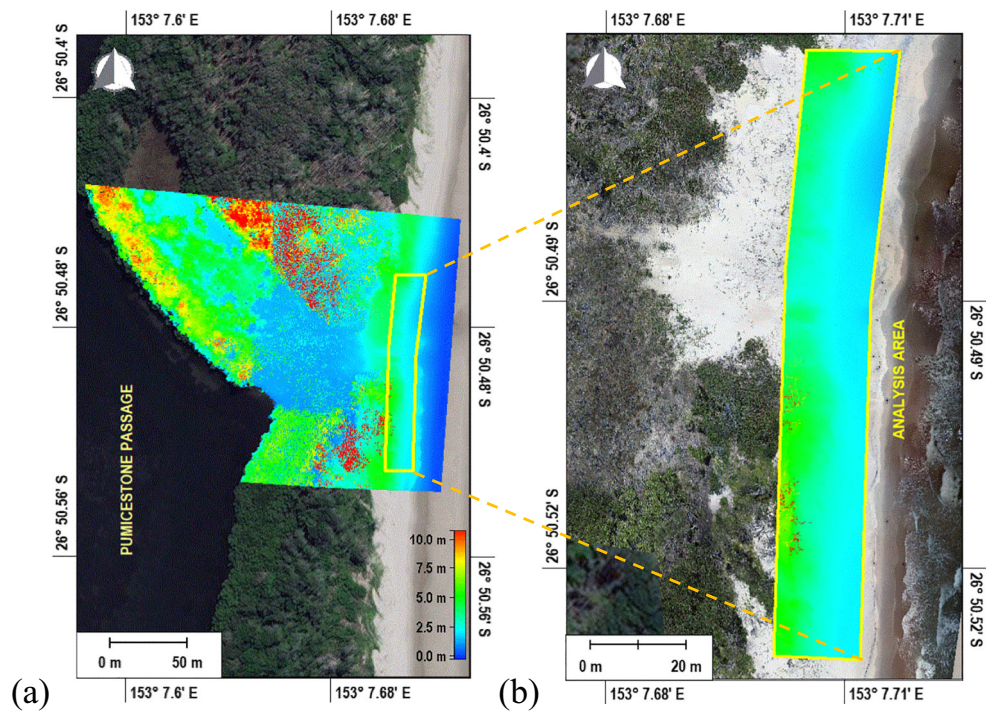
Fig. 7 Example georeferenced point cloud (coloured by elevation) of (**a**) the *Study Area* post-processing with the Python script and (**b**) the portion of the cropped point cloud retained (*Analysis Area*) for detailed analysis (MGA Projection, GDA 94 Datum)


Here, P40 and Hovermap mesh objects of the *Analysis Area* were imported into 3DR where measures of foredune and beach elevation and slope were calculated using Colour Along a Direction (*z*-axis) and Slope Analysis tools (max slope tolerance = 90°), respectively. To aid in the visualization of meaningful differences, the default 'continuous' colourisation scheme was reduced to a user-specified number of 'levels'. Here, thirteen levels were utilized for elevation (one level per 0.5 m difference) and six (one level per 15° difference)

across the slope analysis. Each elevation mesh was then exported in *.asc "Vertices Only" format to retain only the *x*, *y*, and *z* position information for each whilst exporting slope as an ASCII *.ply file retained the position and slope data as calculated by 3DR.

In addition to elevation and slope, 3DR allows a mesh-to-mesh comparison of the difference, or deviation, between two models. Similar to 'DEMS of Difference' comparisons of Le Mauff et al. [40], two meshes were selected and the Compare/Inspect tool was applied with the 'ignore points with a

Fig. 8 Example mesh creation using Hovermap point cloud data from *Survey2* illustrating (**a**) the original point cloud, (**b**) points classified as 'ground', and (**c**) the resulting mesh object (DTM)
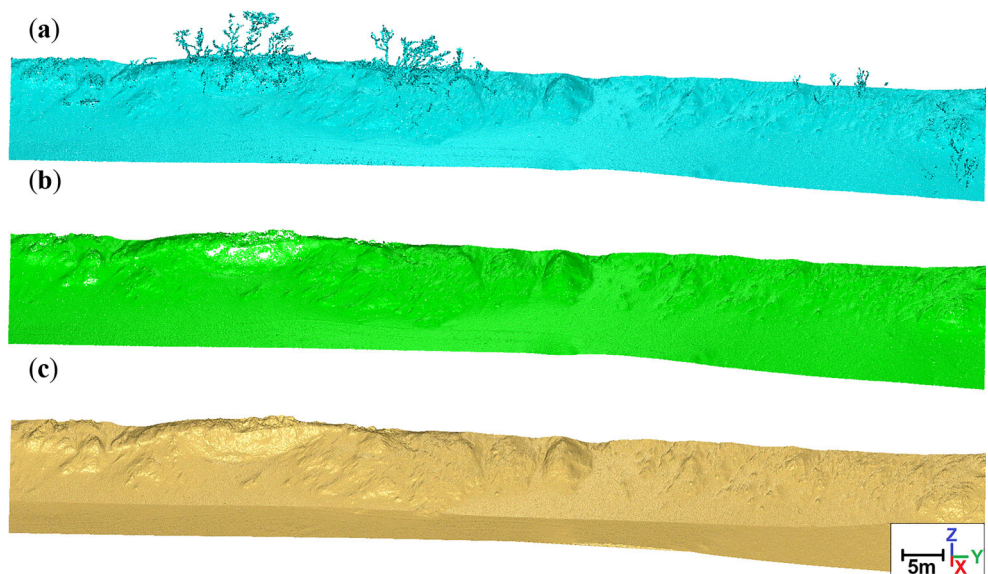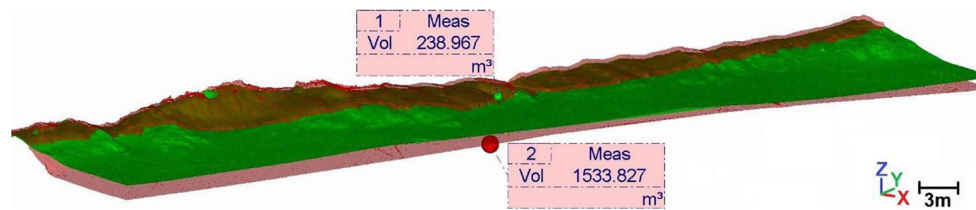
Fig. 9 Example cubature analysis output with observed volumetric differences between *Survey3* (green) and *Survey4* (red) during which approximately (1) 239 m³ of sand was deposited on the dune crest whilst (2) 1534 m³ was removed from undercutting and erosion processes during *Interval3*

distance greater' than function disabled. As we were primarily interested in vertical differences between surveys, the option of applying a 2D inspection along the *z*-axis was utilized. This data was then exported as a *.csv file for further interrogation. This approach is supported by the work of Zhang et al. [70] who indicate that the relative vertical accuracy between the compared DEMs is more important than the absolute estimations derived by comparing each survey to GCPs.

Similar to the analysis of Claudino-Sales et al. [16], Allen et al. [7], and Jaud et al. [34], volumetric differences between mesh models were of interest. As such, the cubature function of 3DR was also utilized along the *z*-axis (user defined) to quantify the approximate volume of sand removed and/or deposited (i.e. below/above reference surface) during each survey interval (Fig. 9). Approximated volumes were recorded directly as displayed within 3DR.

2.10 Data Analysis Structure and Interrogation

In each case, the preceding survey was utilized as the reference surface, with the exception of the P40 to Hovermap comparison (*Survey1*), wherein the P40 data was utilized as the reference model. With each mesh comprised of tens of millions of data points, a simple Python script was written to accept the exported data in the various formats, interrogate for descriptive statistics, and generate histogram data. Microsoft Excel (v.2013, Microsoft Corp., USA) was used to process the marine weather data as well as produce relevant wind roses, histograms and charts.

3 Results

3.1 UAV Flight Performance

As listed in Table 3, UAV flight performance was in line with the prescribed parameters and relatively consistent across all surveys with the exception of the increased altitude observed in *Survey4* with corresponding increase on the observed range and decreased SEV. This is considered unlikely to have been an issue with the UAV platform performance but rather a consequence of changes in foredune topography (lower beach elevation) during *Interval3* as evidenced in the results from the elevation, deviation, and cubature analysis.

3.2 Hovermap Point Clouds

Similar to that of UAV flight performance, the corresponding Hovermap point clouds were all relatively consistent across each survey (Table 4). Analogous to the observations of Sofonia et al. [57], the inverse relationship between altitude/range and point cloud density is evident with corresponding increases in GSD. The relationships between density/SEV and GSD/EDR also appears to hold, however, a greater sample size with repeated measures would be needed to determine the appropriate coefficients and strength of observed correlations.

3.3 Marine Weather

Marine weather data recorded over the study period showed that daily averaged wind speeds ranged from 7.9 to 41.9 m·s⁻¹ ($\overline{x}$ =

Table 3 Descriptive statistics of UAV flight performance over the *Study Area* for each survey

Event	Altitude (m) $\overline{x} \pm \sigma$	Speed (m·s⁻¹) $\overline{x} \pm \sigma$	Range (m) $\overline{x} \pm \sigma$	Pattern (s·m⁻¹)	SEV (s·m⁻²)
Survey1	16.0 ± 3.0	4.0 ± 0.8	21.7 ± 8.2	127	5.9
Survey2	17.1 ± 3.1	4.0 ± 1.6	22.7 ± 8.1	144	6.3
Survey3	17.7 ± 2.8	4.2 ± 0.7	23.8 ± 8.2	121	5.1
Survey4	20.7 ± 2.9	3.9 ± 0.3	26.2 ± 7.6	122	4.7

Table 4 Descriptive statistics of Hovermap point clouds over the *Study Area* for each survey

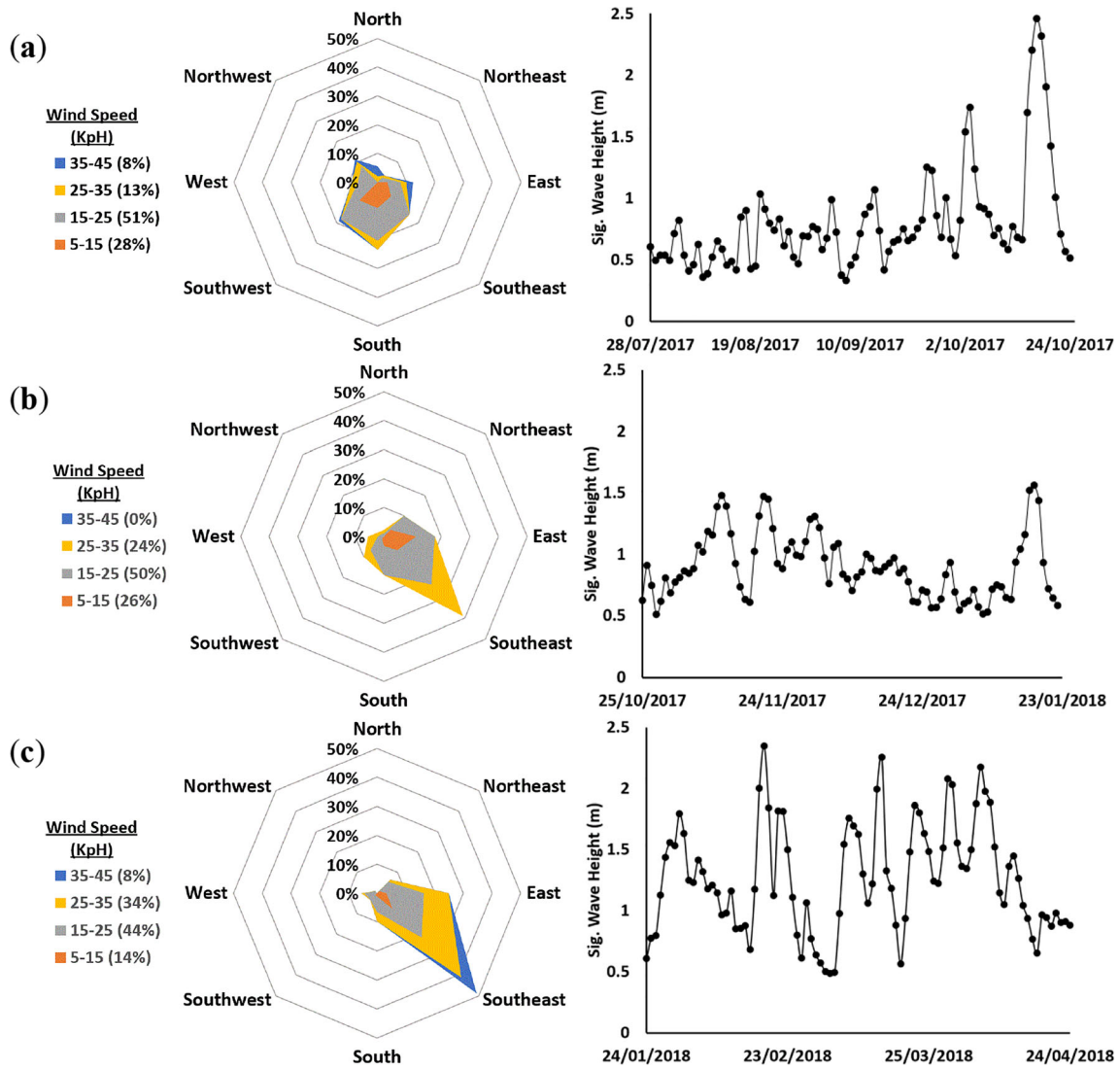| Event	Density (pts·m⁻²)	GSD (m)	ESR (pts·s⁻¹)	EDR (pts·m⁻² s⁻¹)
Survey1	2740	0.019	101,000	2.4
Survey2	2600	0.020	93,000	2.0
Survey3	2420	0.020	93,500	2.2
Survey4	2370	0.021	86,600	2.1

Fig. 10 Daily wind (speed and direction) and significant wave heights recorded between (**a**) *Interval1*, (**b**) *Interval2*, and (**c**) *Interval3*

Table 5 Descriptive statistics for the elevation and slope analysis as well as the mesh-to-mesh comparison of vertical deviation and cubature observed across the *Analysis Area*

(a) Elevation	Survey1-P40	Survey1-HM	Survey2-HM	Survey3-HM	Survey4-HM
Minimum	1.20 m	1.17 m	1.40 m	1.44 m	0.43 m
Maximum	6.43 m	6.48 m	6.63 m	6.70 m	7.00 m
$\bar{x} \pm \sigma$	2.74 ± 0.87 m	2.80 ± 0.97 m	2.93 ± 0.95 m	2.94 ± 0.94 m	2.44 ± 1.49 m
(b) Slope					
Minimum	0.0°	0.0°	0.0°	0.0°	0.0°
Maximum	78.0°	76.0°	89.8°	89.0°	89.9°
$\bar{x} \pm \sigma$	11.2 ± 8.0°	12.1 ± 8.2°	13.1 ± 8.9°	13.6 ± 8.8°	17.3 ± 13.5°
(c) Deviation	Survey1-HM:P40	Survey2:Suvey1-HM	Survey3:Survey2-HM	Survey4:Survey3-HM	
Above ref.	1.57 m	0.62 m	0.73 m	1.14 m	
Below ref.	− 0.68 m	− 0.81 m	− 0.48 m	− 2.26 m	
$x\sigma$	0.01 ± 0.03 m	0.13 ± 0.10 m	0.08 ± 0.06 m	0.74 ± 0.51 m	
(d) Cubature					
Deposition	22.2 m³	295.5 m³	105.4 m³	239.0 m³	
Erosion	− 19.6 m³	− 26.7 m³	− 82.7 m³	− 1533.8 m³	
Net change	2.5 m³	268.7 m³	22.7 m³	− 1294.9 m³	

Fig. 11 Histogram outputs and mesh models of the *Analysis Area* elevation (0.5 m contours), coloured by elevation (m), observed in (**a**) *Survey1-P40* and *Survey1-HM*, (**b**) *Survey2-HM*, (**c**) *Survey3-HM*, and (**d**) *Survey4-HM*. Red dashed box represents the approximate location of the existing blowout
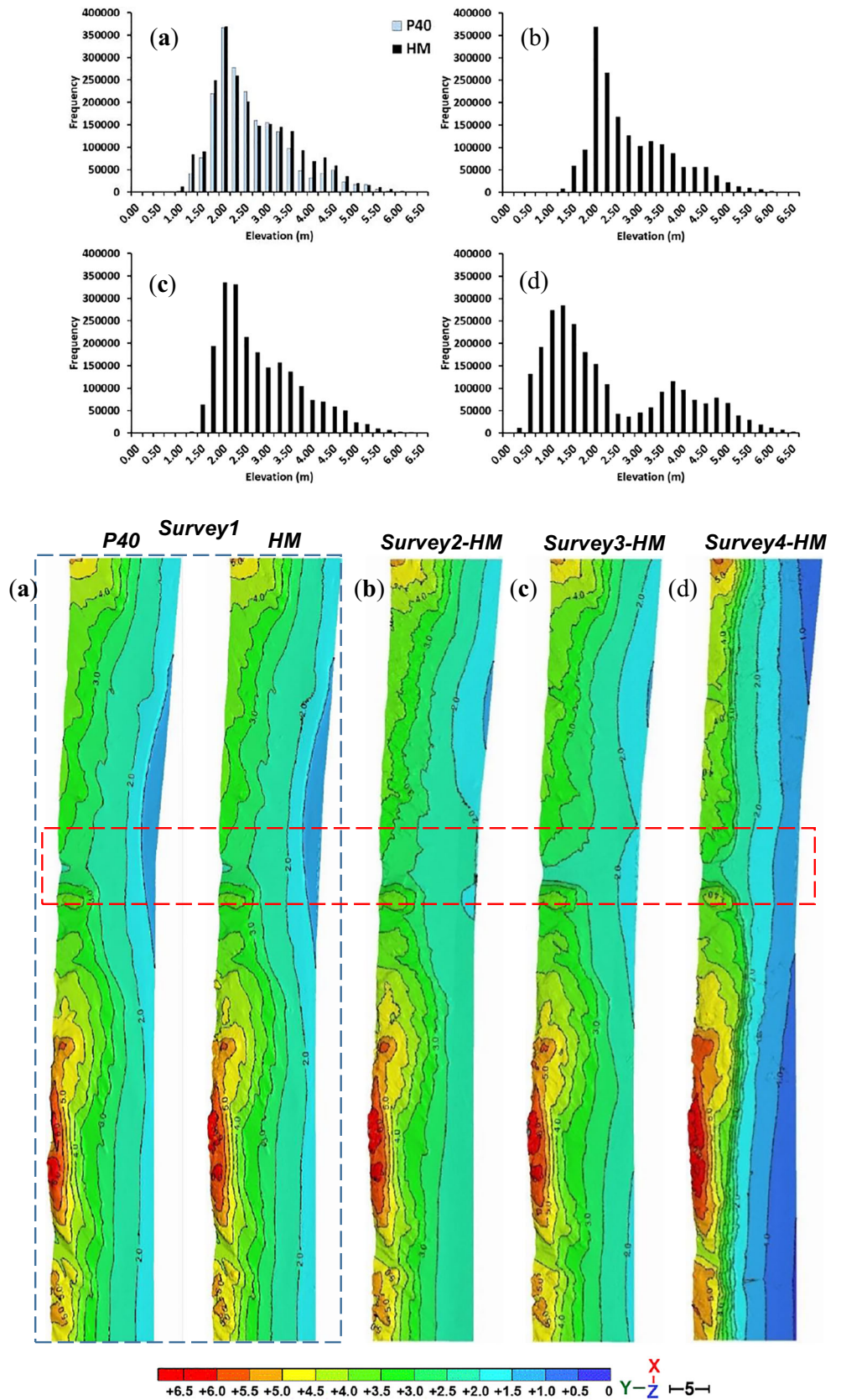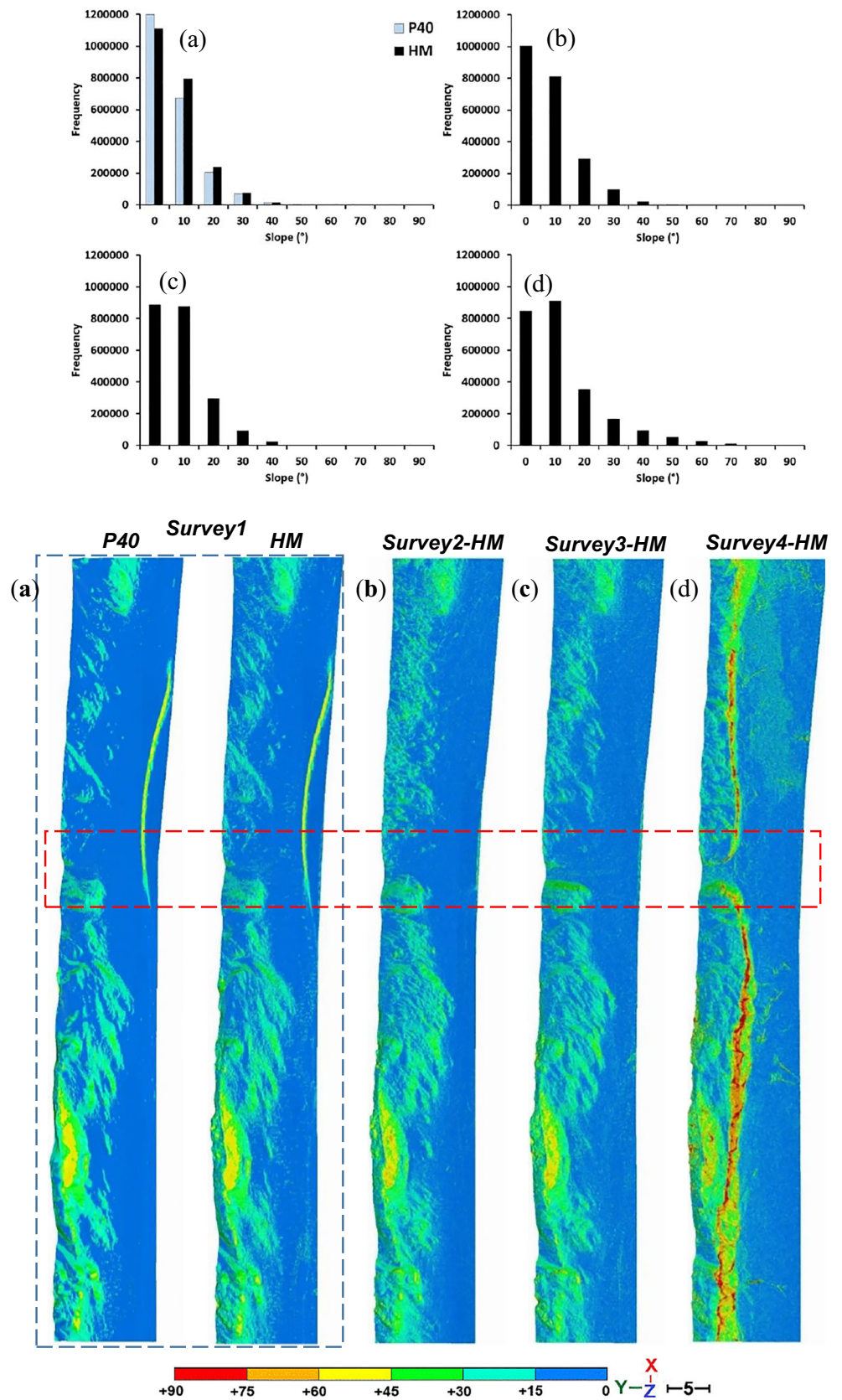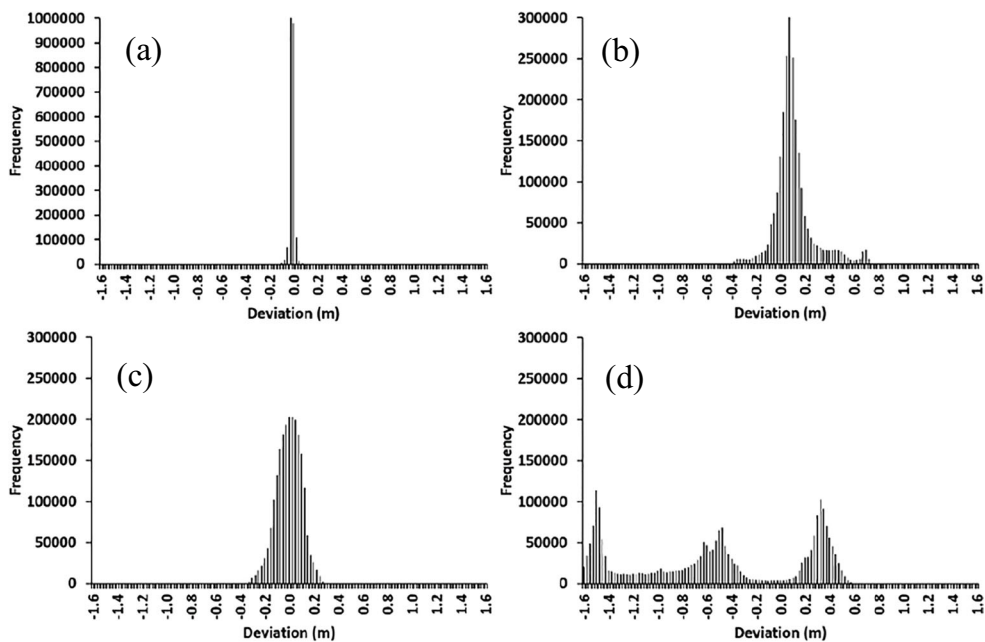
Fig. 12 Histogram outputs and mesh models of the *Analysis Area* slope coloured by degrees (°), observed in (**a**) *Survey1-P40* and *Survey1-HM*, (**b**) *Survey2-HM*, (**c**) *Survey3-HM*, and (**d**) *Survey4-HM*. Red dashed box represents the approximate location of the existing blowout

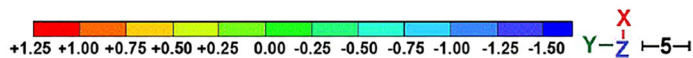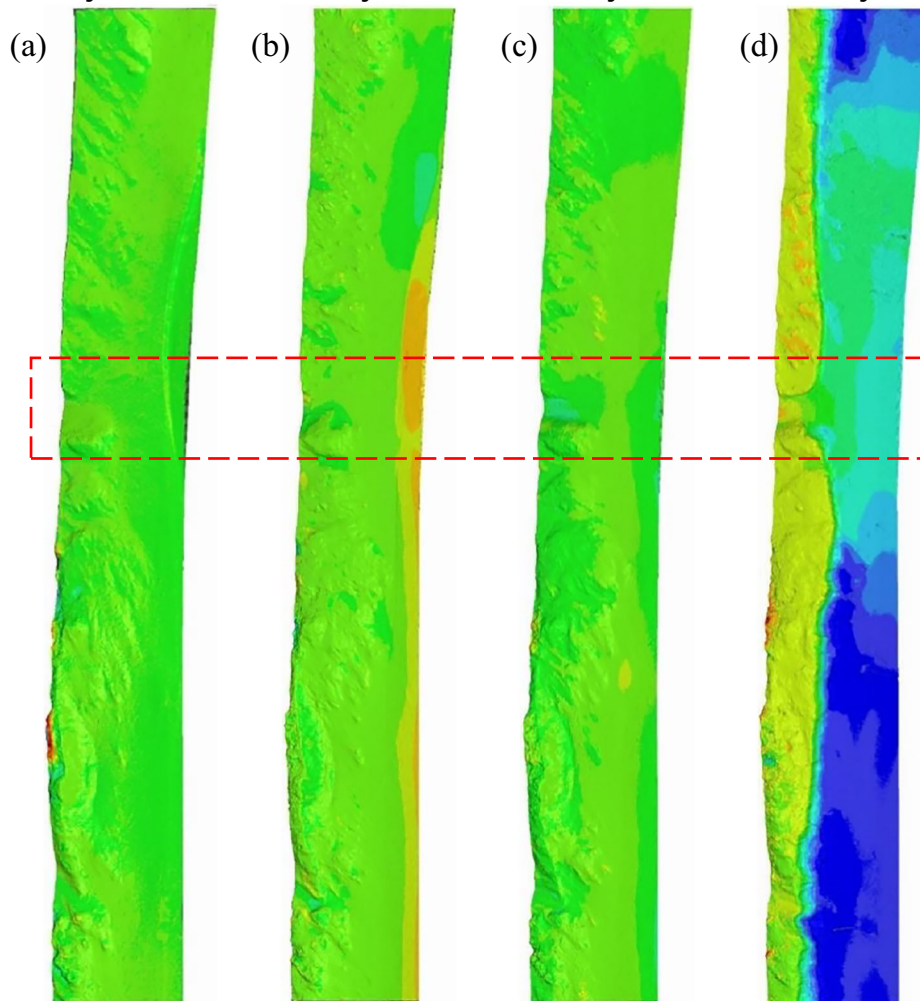Survey1-HM:P40   Survey2:1-HM   Survey3:2-HM   Survey3:4-HM

◀ **Fig. 13** Histogram outputs and mesh models of the *Analysis Area* mesh-to-mesh vertical (*z*-axis) deviation coloured by distance (m) between (**a**) *Survey1-HM:Survey1-P40*, (**b**) *Survey2-HM:Survey1-HM*, (**c**) *Survey3-HM:Survey2-HM*, and (**d**) *Survey4-HM:Survey30-HM*. Red dashed box represents the approximate location of the existing blowout

21.4 ± 7.4 m·s^{-1}) predominantly from the south/southeast with wave heights of 0.3–2.5 m ($\overline{x} = 1.0 \pm 0.4$ m). Although no cyclonic activity occurred at the *Study Area* during this investigation, significantly increased wind speeds (ANOVA, $F(1,180) = 6.257$, $p = 0.013$) and wave heights (ANOVA, $F(1,180) = 41.769$, $p \leq 0.001$) were recorded during *Interval3* (Fig. 10). Descriptive statistics of the marine weather recorded during the study are provided in Table 6, Appendix A.

3.4 Hovermap to P40 Comparison

Values across all measurement matrices, as determined from the *Survey1* Hovermap data (*Survey1-HM*), were very similar to those derived from the P40 'baseline'. This not only demonstrates that Hovermap is comparable to more traditional terrestrial laser scanning techniques within the construct of this study but also provides an indication as to the suitability of this workflow in coastal monitoring applications.

Specifically, minimum, maximum, and mean elevations from *Survey1-HM* were each within the reported ± 1.2 mm accuracy of the P40 (Table 5a). Similarly, the calculated values for slope (Table 5b) were also comparable, varying by approximately 7.4%. Mean deviation of Survey1-HM mesh to P40 mesh was 0.01 ± 0.03 m, consistent with the reported ±30 mm accuracy of the Velodyne sensor (Table 5c) with cubature reporting a net difference of 2.5 m^3 across the *Analysis Area* (Table 5d). Results for elevation, slope, and deviation are also visualized using histograms and associated mesh models of Figs. 13a, 14, and 15a.

3.5 Temporal Change

Temporal variance across the *Analysis Area* was relatively consistent in the measurement matrices over the course of the study, however, considerable changes were evident within the *Survey4-HM* model. Here, mean elevation decreased whilst both slope and deviation measured increased relative to the *Survey3-HM* mesh (Table 5). Most notably, a negative net loss of approximately 1295 m^3 was observed in the cubature analysis during this period. Interestingly, the standard deviations observed relative to the mean values across all measures of *Survey4-HM* data also increased providing
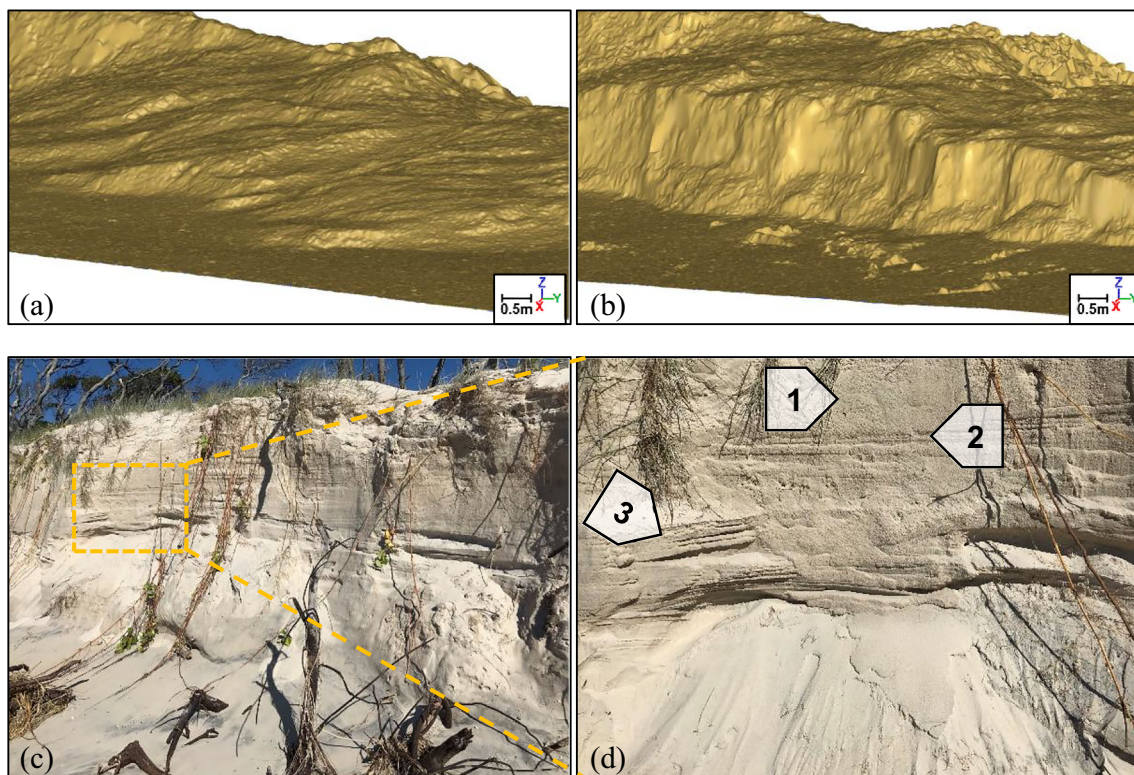

Fig. 14 Example undercutting and scarping of the foredune by storm waves prior during *Interval3* when comparing the same segments of the (**a**) *Survey3-HM* and (**b**) *Survey4-HM*. Photos of this portion of the foredune taken during *Survey4* illustrate (**c**) microscale post-scarp wedge failures with rhizome undermining/exposure and (**d**) earlier dune bedding features including (1) rapid precipitation deposition, (2) reactivation surfaces, and (3) aeolian cross bedding
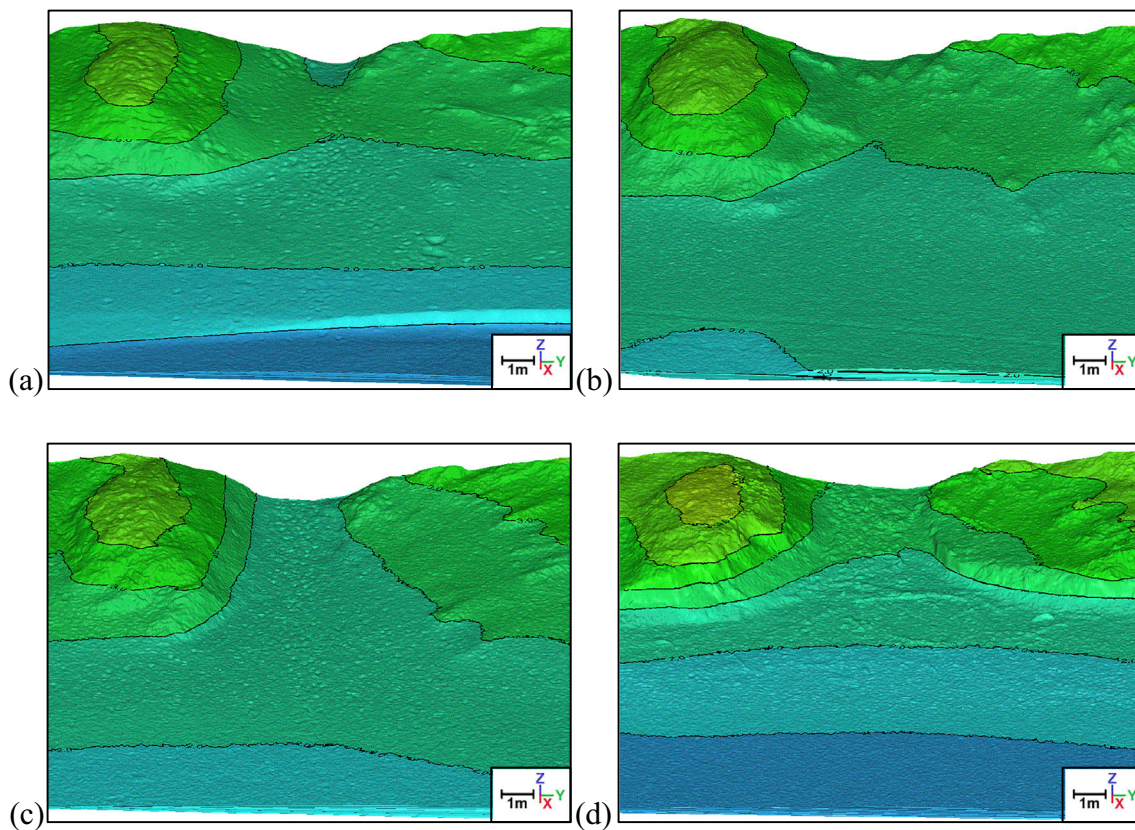
Fig. 15 Topographic change, coloured by elevation (m) at the existing blowout as observed in (**a**) *Survey1-HM*, (**b**) *Survey2-HM*, (**c**) *Survey3-HM*, and (**d**) *Survey4-HM* (0.5 m contour intervals)

further evidence of a transition from a relatively uniform to more complex foredune environment.

These changes are better visualized in the histograms and mesh models of Figs. 13, 14, and 15, wherein an increased distribution of elevation and deviation values is also evident. Correspondingly, tighter topographic contours (Fig. 11d) and slope values greater than 40° were recorded in the *Survey4-HM* mesh (Fig. 12d), reflecting scarping of the foredune during *Interval3*. Whilst an overall decrease deviation values (Fig. 13d) were observed relative to the *Survey3-HM* mesh coinciding with the net volumetric loss of sand measured in the cubature analysis, sand deposition along the dune crest is also evident during this period.

Similar to that described by Short and Hesp [55], Carter and Stone [14], and Sherman and Bauer [54], the dynamic changes observed in *Survey4-HM* are most likely linked with

the process forces associated with the relatively high-energy wind-wave climate recorded during *Interval3*.

3.6 Foredune Scarping and Blowout Area

As evidenced within the *Survey4-HM* mesh, substantial scarping of the foredune occurred during *Interval3*. This is best visualized when illustrating the same segments of the foredune, at reduced scale, and rotated to a perspective view of the stoss slope. Here, the change between *Survey3-H*M (Fig. 14a) and *Survey4-HM* (Fig. 14b) mesh is clearly visible and includes detail such as microscale wedge failures. These observations from the mesh data are supported by photographs of this section of the foredune during *Survey4* (Fig. 14c, d).

Fig. 16 Photomosaic image of the *Analysis Area* illustrating dark sands (lower right) indicating the presence of 'coffee rock' near the beach surface
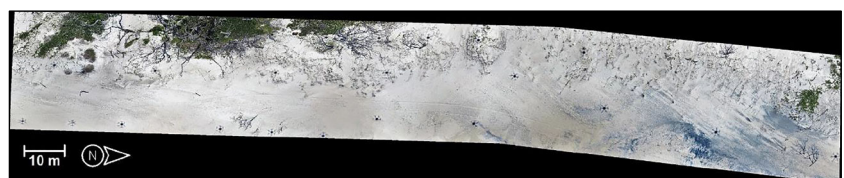
Similar to that observed across the *Analysis Area*, temporal change was also observed at the existing blowout. As illustrated in Fig. 15, relatively minor changes in elevation and slope (as perceived through 0.5 m contours) were detected through most of the study with the exception of *Survey4-HM* where scarping of the foredune and lowering of the beach were evident (Fig. 15d). Interestingly, the highest elevation (~ 4.1 m) of the blowout (southern ("-Y") side of blowout trough) was also observed in *Survey4-HM* mesh associated with sand deposition on the dune crest. In addition, sand was deposited at the back of the trough slightly raising the elevation of this portion of the blowout compared with the *Survey3-HM* mesh.

Although heavy scarping occurred along the foredune during *Interval3* resulting in the steepening of the trough walls, the depth of the blowout remained relatively unchanged (min. ~ 2.2 m) throughout the course of the study. This suggests the presence of a deflation floor at, or near, this elevation that is potentially linked to the water table of Pumicestone Passage, an immobile layer of rock and/or, semi-permanent layer of shell, or gravel representing a deflation limit of this blowout and washover features of the foredune [13].

4 Discussion

Cracknell [18] stated that the key to success, or otherwise, of remote sensing in coastal or estuarine studies lies in the question of scale. Successful in mapping, detecting, and quantifying change on centimetre-level scales, with accuracy consistent with more traditional terrestrial laser scanning (TLS) techniques, results from this study demonstrate that the UAV LiDAR, such as the Hovermap, has strong potential as a tool for future research and monitoring of coastal dunes and other dynamic geomorphic systems.

4.1 Hovermap Performance Comparison

Similar to the UAV SfM work of Papakonstantinou et al. [48], we presented a UAV LiDAR workflow that facilitates the study of coastal changes, and accurate visualization of 3D models, of the beach and foredune over micro spatial and temporal scales. With regard to performance, the Hovermap reported a mean point cloud density of 2532 ± 170 pts.·m^{-2} and GSD of 0.02 ± 0.001 m across the *Study Area*. As a byproduct of the relatively low altitudes and flight speeds [57], the resolution achieved here was substantially higher than the 1–30 pts.·m^{-2} and 0.3–0.5 m GSD traditionally associated with airborne LiDAR from manned aircraft [6, 39, 45, 69]. The cost, however, is realized in the relatively limited spatial scales that can be achieved by UAVs compared with that of manned aircraft.

A closer comparison, therefore, may be made relative to previous UAV SfM studies where again the Hovermap reported consistently higher spatial resolution. Goncalves and Henriques [26], for example, reported 0.032–0.45 m resolution, whilst Jaud et al. [34] evidenced a 'high' spatial resolution of 0.042 m·px^{-1}. Similarly, resolution up to 0.047 m·px^{-1} were reported by both Papakonstantinou et al. [48] and Topouzelis et al. [61]. Of the studies reviewed, only the work of Guillot and Pouget [28] described a spatial resolution (0.015 m·px^{-1}) greater than what was observed in this study.

With a mean RMSE of 0.050 ± 0.31 m, the absolute accuracy of the Hovermap point clouds to GCP targets were again consistent with the 0.02–0.8 m range reported in previous manned airborne LiDAR [6, 39, 43] and UAV SfM (0.17–0.3 m) studies [17, 34, 44, 61]. According to Le Mauff et al. [40], these relatively small differences may be attributed to noise inherent to LiDAR data.

4.2 Foredune Scarping and Blowout Area

The Hovermap performance enabled the mesh models utilized here to be created with polygon size of 0.02 m and fine-scale evaluations of foredune elevation and slope as well as change detection between survey events in the deviation and cubature analysis. Utilizing the methodology in point cloud processing and mesh creation described, both nominal and substantial temporal changes in foredune were observed throughout the study with the exception of *Survey4-HM* data where substantial changes in the foredune were evidenced. According to Brown and McLachlan [11], physical features of beaches reflect the interaction of wave height, wavelength, and direction of the tidal regime and sediment transport available impacting sandy beaches either directly through changes in the structure of vegetation or substratum. Here, we estimated that a net loss of approximately 1295 m^3 of sand was removed from the *Analyis Area* during *Interval3* and observed corresponding increases in the maximum elevation, slope, and deviation from previous surveys. This measure of sand loss and deviation are supported by the marine weather data recorded during *interval3* and correlations between storms, wind direction, wave heights, and erosional processes of numerous previous studies [14, 16, 19, 23, 37]. Similarly, in accordance with Arens [8], the increase in maximum elevation and mean slope may be contributed to scarping of the foredune and corresponding loss of vegetation where sand is transported further up the stoss faces, and this can increase as foredune height and/or steepness increases. Continued monitoring was beyond the scope of this study; however, subsequent foredune recovery will likely depend on the degree of revegetation and timeframes associated with reestablishment [52].

As described by Hesp [30], the existing blowout and overwash fan within the *Study Area* were likely formed by wave erosion along the seaward face of the dune with overwash hollows and fans developing into blowouts if the vegetation cover is slow in reestablishing. Interestingly, the blowout studied here demonstrated relatively minor changes

in elevation and slope through most of the study with the exception of *Survey4-HM* where scarping of the foredune and lowering of the beach was evident with increased maximum elevations and slopes observed and consistent with trough-blowout topography that can significantly accelerate wind speeds along the deflation floor and lateral erosion walls resulting in steep stoss faces and general elongation of the blowout [31, 32]. Interestingly, the depth of the blowout remained relatively unchanged (min. ~ 2.2 m) throughout the course of the study and suggested this elevation represents the deflation limit of this blowout [13]. Chapman [15] described a 'coffee rock' layer underlying unconsolidated sands at Bribie Island that may be associated with the deflation limit observed. Evidence for this is presented in Fig. 16, where the dark sands along the lower right of the image of the *Analysis Area* indicate the presence of the coffee rock layer near the beach surface.

4.3 Limitations and Future Research

Repeatability is a function of the stability of calibration of the instrument, accuracy of position estimation (either via GNSS or SLAM), density and completeness of point cloud coverage, and the availability and accuracy of 'ground-truth' information [29]. In this study, the Velodyne sensor and Hovermap system were both calibrated by the manufacturers and stable over the course of the study. At over 2000 pts.·m^{-2}, point cloud density was consistently high and the 'cross-flight' pattern utilized ensured complete coverage of the *Study Area* during each survey. Lague et al. [38] reported that the primary sources of uncertainty in point cloud comparison are within the registration uncertainty between point clouds. Here, referencing individual point clouds to the GCPs introduced error, however, observed RMSE values were similar to values reported in airborne LiDAR from manned aircraft. Additional potential sources of error include the accuracy associated with the data collection process (i.e. robustness of the SLAM solution) and that associated with the topographic interpolation process action [37]. This is supported by Grohmann and Sawakuchi [27] who discussed the influence of DTM cell size on volumetric calculations and observed a directly proportional increase in RMSE and cell size.

The approach described here is likely to be particularly useful at microspatial and temporal scales and, similar to the work of Simpson et al. [56], may be expanded to include additional attributes of the coastal dune environment such as detecting changes in vegetation structure. Specifically, elaboration on the work of Lalimi et al. [39] though the application of UAV LiDAR could assess if derived leaf area indices improve from point cloud data that is several orders of more dense magnitude. It would also be interesting to regularly deploy UAV LiDAR over longer periods to evaluate the utility of high-spatial resolution data in the correlation of marine weather and coastal dune formation, blowout formation, and subsequent recovery processes. Such predictive modelling would also likely benefit on having high-frequency, multi-temporal data microscales to inform morphodynamic and beach dune erosion models.

5 Conclusions

Although, additional work is required to better understand point cloud response under different site conditions, the results demonstrated here confirm that UAV LiDAR is a robust tool and has great promise as a new tool among the various methods currently available to coastal scientists and engineers. The high spatial resolution and flexibility of deployment are key attributes to UAV remote sensing and will likely better inform future theories, models, and predictions, particularly on microtemporal and spatial scales. We believe the methods for evaluation described here could be applied to other UAV LiDAR systems and compared with more traditional techniques to assist future operators in better understanding system performance, and limitations, and thereby inform cost/benefit decisions when selecting instrumentation for future coastal geomorphology studies.

Compliance with Ethical Standards

Conflict of Interest The authors declare that they have no conflict of interest.

Appendix

Table 6 Descriptive statistics and ANOVA results from the examination of (a–d) daily wind speed and (e–h) daily significant wave height recorded between each survey and overall study period

	Min	Max	$\bar{x} \pm \sigma$	ANOVA
Daily wind speed				
Interval1	9.8 m s^{-1}	41.9 m s^{-1}	20.7 ± 7.9 m s^{-1}	–
Interval2	9.8 m s^{-1}	34.2 m s^{-1}	20.4 ± 6.5 m s^{-1}	$F(1,177) = 0.102, p = 0.750$
Interval3	7.9 m s^{-1}	39.7 m s^{-1}	23.0 ± 7.5 m s^{-1}	$F(1,180) = 6.257, p = 0.013$
Total study period	7.9 m s^{-1}	41.9 m s^{-1}	21.4 ± 7.4 m s^{-1}	$F(1,268) = 3.388, p = 0.035$
Daily sig. wave height				
Interval1	0.3 m	2.5 m	0.8 ± 0.4 m	–
Interval2	0.5 m	1.5 m	0.9 ± 0.2 m	$F(1,177) = 3.891, p = 0.050$
Interval3	0.5 m	2.5 m	1.3 ± 0.5 m	$F(1,180) = 41.769, p \leq 0.001$
Total study period	0.3 m	2.5 m	1.0 ± 0.4 m	$F(1,268) = 35.234, p \leq 0.001$

References

1. Queensland Govvernment (2010) Moreton Bay Marine Park User Guide from the Marine Parks (Moreton Bay) Zoning Plan 2008. Available online: https://www.npsr.qld.gov.au/parks/moreton-bay/zoning/pdf/marine-park-user-guide.pdf. Accessed 14 August 2018. The State of Queensland Department of State Development, 2-40

2. Queensland Government (2017) Queensland Government Department of Environment and Science-parks and forests. Available online: www.npsr.qld.gov.au/parks/bribie-island/about. Accessed 21 July 2017

3. Australian Government (2018) Australian Government, Bureau of Meteorology. Latest Weather Observations for Spitfire Channel (Station 040927). Available online: www.bom.gov.au/products/IDQ60801/IDQ60801.94581.shtml. Accessed 25 April 2018

4. Leica Geosystems (2018) Leica Geosystems. Leica Viva GS16 GNSS Smart Antenna. Data Sheet. Available online: https://leica-geosystems.com/products/gnss-systems/smart-antennas/leica-viva-gs16. Accessed on 25 July 2018

5. Queensland Government (2018) Queensland Government, Department of Science, Information Technology, and Innovation-Science Division, Coastal Impacts Unit, Monitoring Team. Available online: https://data.qld.gov.au/dataset/coastal-data-system-waves-caloundra. Accessed 17 August 2018

6. Abhar KC, Walker IJ, Hesp PA, Gares PA (2015) Spatial-temporal evolution of aeolian blowout dunes at Cape Cod. Geomorphology 236:148–162

7. Allen TR, Oertel GF, Gares PA (2012) Mapping coastal morphodynamics with geospatial techniques, Cape Henry, Virginia, USA. Geomorphology 137:138–149

8. Arens SM (1996) Patterns of sand transport on vegetated foredunes. Geomorphology 17:339–350

9. Brock J, Sallenger A, Krabill W, Swift R, Manizade S, Meredith A, Jansen M, Eslinger D (1999) Aircraft laser altimetry for coastal process studies. Amer Soc Civil Engineers, New York

10. Brock JC, Purkis SJ (2009) The emerging role of Lidar remote sensing in coastal research and resource management. J Coast Res 25:1–5

11. Brown AC, McLachlan A (2002) Sandy shore ecosystems and the threats facing them: some predictions for the year 2025. Environ Conserv 29:62–77

12. Brownett JM, Mills RS (2017) The development and application of remote sensing to monitor sand dune habitats. J Coast Conserv 21: 643–656

13. Carter RWG, Hesp PA, Nordstrom KF (1990) Erosional landforms in coastal dunes. In: Nordstrom KF, Psuty NP, Carter RWG (eds) Coastal dunes: form and process. Wiley, London, pp 217–250

14. Carter RWG, Stone GW (1989) Mechanisms associated with the erosion of sand dune cliffs, Magillian, Northern-Ireland. Earth Surf Process Landf 14:1–10

15. Chapman S (2010) Climate proofing Bribie: a climate adaptation action plan. SEQ Catchments

16. Claudino-Sales V, Wang P, Horwitz MH (2010) Effect of hurricane Ivan on coastal dunes of Santa Rosa Barrier Island, Florida: characterized on the basis of pre- and poststorm LiDAR Surveys. J Coast Res 26:470–484

17. Cook KL (2017) An evaluation of the effectiveness of low-cost UAVs and structure from motion for geomorphic change detection. Geomorphology 278:195–208

18. Cracknell AP (1999) Remote sensing techniques in estuaries and coastal zones-an update. Int J Remote Sens 20:485–496

19. Davidson MA, Turner IL, Splinter KD, Harley MD (2017) Annual prediction of shoreline erosion and subsequent recovery. Coast Eng 130:14–25

20. Dong PL (2015) Automated measurement of sand dune migration using multi-temporal LiDAR data and GIS. Int J Remote Sens 36: 5426–5447

21. Elsner P, Dornbusch U, Thomas I, Amos D, Bovington J, Horn D (2018) Coincident beach surveys using UAS, vehicle mounted and airborne laser scanner: point cloud inter-comparison and effects of surface type heterogeneity on elevation accuracies. Remote Sens Environ 208:15–26

22. Emesent (2018) Hovermap LiDAR system: product specification. Available online: https://emesent.io/products.html. Accessed 23 November 2018

23. Fabbri S, Giambastiani BMS, Sistilli F, Scarelli F, Gabbianelli G (2017) Geomorphological analysis and classification of foredune ridges based on Terrestrial Laser Scanning (TLS) technology. Geomorphology 295:436–451

24. Gerke M, Przybilla HJ (2016) Accuracy analysis of photogrammetric UAV image blocks: influence of onboard RTK-GNSS and cross flight patterns. Photogramm Fernerkund Geoinf, 17-30

25. Girardeau-Montaut D (2016) CloudCompare - Open Source Project. Available online: http://www.danielgm.net/cc/. Accessed 16 October 2017

26. Goncalves JA, Henriques R (2015) UAV photogrammetry for topographic monitoring of coastal areas. ISPRS-J Photogramm Remote Sens 104:101–111

27. Grohmann CH, Sawakuchi AO (2013) Influence of cell size on volume calculation using digital terrain models: a case of coastal dune fields. Geomorphology 180:130–136

28. Guillot B, Pouget F (2015) UAV application in coastal environment, example of the Oleron Island for dunes and dikes survey. In: Mallet C, Paparoditis N, Dowman I, Elberink SO, Raimond AM, Sithole G, Rabatel G, Rottensteiner F, Briottet X, Christophe S, Coltekin A, Patane G (eds) Isprs geospatial week 2015. Copernicus Gesellschaft Mbh, Gottingen, pp 321–326

29. Gutierrez J, Gibeaut JC, Smyth RC, Hepner TL, Andrews JR (2001) Precise airborne LiDAR surveying for coastal research and geohazards applications. International Archives of Photogrammetry and Remote Sensing XXXIV-3W4:22–24

30. Hesp P (2002) Foredunes and blowouts: initiation, geomorphology and dynamics. Geomorphology 48:245–268

31. Hesp PA (1996) Flow dynamics in a trough blowout. Bound-Layer Meteor 77:305–330

32. Hesp PA, Hyde R (1996) Flow dynamics and geomorphology of a trough blowout. Sedimentology 43:505–525

33. Hugenholtz CH, Whitehead K, Brown OW, Barchyn TE, Moorman BJ, LeClair A, Riddell K, Hamilton T (2013) Geomorphological mapping with a small unmanned aircraft system (sUAS): feature detection and accuracy assessment of a photogrammetrically-derived digital terrain model. Geomorphology 194:16–24

34. Jaud M, Grasso F, Le Dantec N, Verney R, Delacourt C, Ammann J, Deloffre J, Grandjean P (2016) Potential of UAVs for monitoring mudflat morphodynamics (application to the Seine Estuary, France). ISPRS Int. Geo-Inf. 5:20

35. Kalacska M, Chmura GL, Lucanus O, Berube D, Arroyo-Mora JP (2017) Structure from motion will revolutionize analyses of tidal wetland landscapes. Remote Sens Environ 199:14–24

36. Kaul L, Zlot R, Bosse M (2016) Continuous-time three-dimensional mapping for micro aerial vehicles with a passively actuated rotating laser scanner. J Field Robotics 33:103–132

37. Kratzmann MG, Hapke CJ (2012) Quantifying anthropogenically driven morphologic changes on a barrier island: Fire Island National Seashore, New York. J Coast Res 28:76–88

38. Lague D, Brodu N, Leroux J (2013) Accurate 3D comparison of complex topography with terrestrial laser scanner: application to the Rangitikei canyon (N-Z). ISPRS-J. Photogramm. Remote Sens. 82: 10–26

39. Lalimi FY, Silvestri S, Moore LJ, Marani M (2017) Coupled topographic and vegetation patterns in coastal dunes: remote sensing observations and ecomorphodynamic implications. J Geophys Res-Biogeosci 122:119–130

40. Le Mauff B, Juigner M, Ba A, Robin M, Launeau P, Fattal P (2018) Coastal monitoring solutions of the geomorphological response of beach-dune systems using multi-temporal LiDAR datasets (Vendee coast, France). Geomorphology 304:121–140

41. Leica_Geosystems (2015) Leica ScanStation P30/P40. Hexagon AB. Product Specification. Available online: https://leica-geosystems.com/products. Accessed 1 August 2018

42. Levin N (2011) Climate-driven changes in tropical cyclone intensity shape dune activity on Earth's largest sand island. Geomorphology 125:239–252

43. Loftis JD, Wang HV, DeYoung RJ, Ball WB (2016) Using LiDAR elevation data to develop a topobathymetric digital elevation model for sub-grid inundation modeling at Langley Research Center. J Coast Res 134-148

44. Mancini F, Dubbini M, Gattelli M, Stecchi F, Fabbri S, Gabbianelli G (2013) Using unmanned aerial vehicles (UAV) for high-resolution reconstruction of topography: the structure from motion approach on coastal environments. Remote Sens 5:6880–6898

45. Mitasova H, Overton MF, Recalde JJ, Bernstein DJ, Freeman CW (2009) Raster-based analysis of coastal terrain dynamics from multitemporal LiDAR data. J Coast Res 25:507–514

46. Moore AB, Morris KP, Blackwell GK, Jones AR, Sims PC (2003) Using geomorphological rules to classify photogrammetrically-derived digital elevation models. Int J Remote Sens 24:2613–2626

47. Moreno-Casasola P (1986) Sand movement as a factor in the distribution of plant-communities in a coastal dune system. Vegetatio 65:67–76

48. Papakonstantinou A, Topouzelis K, Pavlogeorgatos G (2016) Coastline zones identification and 3D coastal mapping using UAV spatial data. ISPRS Int Geo-Inf 5:14

49. Pikelj K, Ruzic I, Ilic S, James MR, Kordic B (2018) Implementing an efficient beach erosion monitoring system for coastal management in Croatia. Ocean Coastal Manage 156:223–238

50. Revell DL, Dugan JE, Hubbard DM (2011) Physical and ecological responses of sandy beaches to the 1997-98 El Nino. J Coast Res 27: 718–730

51. Ritchie W (1972) The evolution of coastal sand dunes. Scott Geogr Mag 88:19–35

52. Saunders, K.E., Davidson-Arnott, R.G.D., 1990. Coastal dune reponse to natural disturbances. Proceedings on Coastal Sand Dunes. NRC, Ottawa., 32-345

53. Scarelli FM, Cantelli L, Barboza EG, Rosa M, Gabbianelli G (2016) Natural and anthropogenic coastal system comparison using DSM from a low cost UAV survey (Capao Novo, RS/Brazil). J Coast Res 1232-1236

54. Sherman DJ, Bauer BO (1993) Dynamics of beach-dune systems. Prog Phys Geogr 17:413–447

55. Short AD, Hesp PA (1982) Wave, beach and dune interactions in southeastern Australia. Mar Geol 48:259–284

56. Simpson JE, Smith TEL, Wooster MJ (2017) Assessment of errors caused by forest vegetation structure in airborne LiDAR-derived DTMs. Remote Sens 9:18

57. Sofonia J, Phinn S, Roelfsema C, Kendoul F, Rist Y (2019) Modelling the effects of fundamental UAV flight parameters on LiDAR point clouds to facilitate objectives-based planning. ISPRS-J. Photogramm. Remote Sens. In Press - Accepted 18/01/2019

58. Splinter KD, Kearney ET, Turner IL (2018) Drivers of alongshore variable dune erosion during a storm event: observations and modelling. Coast Eng 131:31–41

59. Stockdon HF, Sallenger AH, List JH, Holman RA (2002) Estimation of shoreline position and change using airborne topographic LiDAR data. J Coast Res 18:502–513

60. Tomlinson R (2002) Beaches our asset. Planning and management for natural variability on open coastlines. Proceedings of the Pulic Workshop "Beach Protection and Management". Yeppoon 2002. CRC for Coastal Zone, Estuary and Water Management and Faculty of Engineering and Physical Systems. Ed. J. Piorewisz., 7-33

61. Topouzelis K, Papakonstantinou A, Doukari M (2017) Coastline change detection using unmanned aerial vehicles and image processing techniques. Fresenius Environ Bull 26:5564–5571

62. Turner IL, Harley MD, Drummond CD (2016) UAVs for coastal surveying. Coast Eng 114:19–24

63. van Rossum G (1995) Python Software Foundation. Python Language Reference, version 3.6.4. Available online: http://www.python.org. Accessed 14 February 2018

64. Velodyne_LiDAR (2016) Velodyne LiDAR 'Puck' LITE Light Weight Real-Time 3D Velodyne LiDiAR, 2018. LiDAR Sensor: Product Specification. Available online: http://velodynelidar.com/vlp-16-lite.html. Accessed 1 May 2018

65. Wallace LO, Lucieer A, Watson CS (2012) Assessing the feasibility of UAV-based LiDAR for high resolution forest change detection, Xxii Isprs Congress, Technical Commission Vii. Copernicus Gesellschaft Mbh, Gottingen, pp. 499–504

66. Whitehead K, Hugenholtz C (2014) Remote sensing of the environment with small unmanned aircraft systems (UASs), part 1: a

review of progress and challenges. Journal of Unmanned Vehicle Systems 2:69–85

67. Wright LD, Chappell J, Thom BG, Bradshaw MP, Cowell P (1979) Morphodynamics of reflective and dissipative beach and inshore systems: Southeastern Australia. Mar Geol 32:105–140
68. Wright LD, Short AD (1984) Morphodynamic variability of surf zones and beaches-a synthesis. Mar Geol 56:93–118
69. Young AP, Flick RE, Gutierrez R, Guza RT (2009) Comparison of short-term seacliff retreat measurement methods in Del Mar, California. Geomorphology 112:318–323

70. Zhang Q, Qin RJ, Huang X, Fang Y, Liu L (2015) Classification of ultra-high resolution orthophotos combined with DSM using a dual morphological top hat profile. Remote Sens 7:16422–16440
71. Zhou X, Wang GQ, Bao Y, Xiong L, Guzman V, Kearns TJ (2017) Delineating beach and dune morphology from massive terrestrial laser-scanning data using generic mapping tools. J Surv Eng-ASCE 143:21